



Journal of Geophysical Research: Atmospheres

RESEARCH ARTICLE

10.1002/2014JD021833

This article is companion to *Baumgarten* and *Fritts* [2014] doi:10.1002/2014JD021832.

Key Points:

- NLC observations are a valuable tracer of small-scale dynamics in the MLT
- Modeling can greatly aid the interpretation of KHI observed in NLC
- Observations and modeling suggest a turbulent viscosity that may be large

Correspondence to:

D. C. Fritts, dave@gats-inc.com

Citation:

Fritts, D. C., G. Baumgarten, K. Wan, J. Werne, and T. Lund (2014), Quantifying Kelvin-Helmholtz instability dynamics observed in noctilucent clouds: 2. Modeling and interpretation of observations, *J. Geophys. Res. Atmos.*, 119, 9359–9375, doi:10.1002/2014JD021833.

Received 27 MAR 2014 Accepted 17 JUL 2014 Accepted article online 19 JUL 2014 Published online 7 AUG 2014

Quantifying Kelvin-Helmholtz instability dynamics observed in noctilucent clouds: 2. Modeling and interpretation of observations

David C. Fritts¹, Gerd Baumgarten², Kam Wan¹, Joseph Werne³, and Tom Lund³

¹Boulder Division, GATS, Boulder, Colorado, USA, ²Leibniz-Institute of Atmospheric Physics, Kühlungsborn, Germany, ³Northwest Research Associates, Boulder, Colorado, USA

Abstract A companion paper describes high-resolution, ground-based imaging of apparent Kelvin-Helmholtz instabilities (KHI) observed in noctilucent clouds (NLCs) near the polar summer mesopause. Here we employ direct numerical simulations of KHI at Richardson numbers from Ri = 0.05 to 0.20 and relatively high Reynolds numbers to illustrate the dependence of KHI and secondary instabilities on these quantities and interpret and quantify the KHI events described by Baumgarten and Fritts (2014). We conclude that one event triggered by small-scale gravity waves provides clear evidence of strong KHI initiated at $Ri \sim 0.05-0.10$. Events arising in a more uniform shear environment exhibit KHI and small-scale dynamics that compare reasonably well with modeled KHI initiated at $Ri \sim 0.20$. Our application of numerical modeling in quantifying KHI dynamics observed in NLCs suggests that characteristics of KHI, and perhaps other small-scale dynamics, that are defined well in NLC displays can be used to quantify the dynamics and spatial scales of such events with high confidence. Specifically, our comparisons of KHI observations and modeling appear to indicate a "turbulent" viscosity $\sim 5-40$ times the true kinematic viscosity at the NLC altitude. This offers an alternative, or an augmentation, to more traditional radar, lidar, and/or airglow measurements employed for such studies of small-scale dynamics at coarser spatial scales during polar summer.

1. Introduction

A companion paper by *Baumgarten and Fritts* [2014] provides an overview of the dynamics yielding small-scale instabilities in the mesosphere and lower thermosphere (MLT), their roles in the transport and deposition of energy and momentum, and the challenges in quantifying these dynamics with existing ground-based MLT instruments. BF14 also note the potential advantages of using noctilucent clouds (NLCs) as a more sensitive tracer of small-scale dynamics than airglow imagers due to their thinner optical layer depth. They then employ this method to illustrate several examples of Kelvin-Helmholtz (KH) instabilities (or KHI) at scales for which these dynamics, including secondary instabilities and the transition to turbulence, can be identified in the NLC images.

Our purposes in this paper are twofold. We first describe KHI and secondary instability dynamics spanning plausible ranges of Richardson numbers (*Ri*) for the KHI events described by BF14. This employs previous direct numerical simulations (DNS) and a large-eddy simulation (LES) of KHI dynamics to characterize KH billow depths, secondary instability structures, and the evolutions of turbulence and mixing as functions of *Ri* and Reynolds number (*Re*). Our second purpose is to apply these DNS and LES results in interpreting two of the KHI events identified by BF14. This reveals a surprising ability to quantify these KHI dynamics based entirely on the NLC imaging and to a degree not possible using other measurement methods. Our numerical methods are described in section 2. Section 3 provides an overview of the DNS and LES results for representative *Ri* and *Re*. Section 4 applies these results to the interpretation of the two events described by BF14 at smaller and larger apparent *Ri*. We discuss the broader implications of these results in section 5. Section 6 provides our summary and conclusions.

2. Numerical Modeling of KHI and Representation of NLC Responses

2.1. Numerical Modeling of KHI

Our initial high-resolution numerical studies of KHI [Werne and Fritts, 1999, 2001; Fritts et al., 2003; Werne et al., 2005] employed a pseudo-spectral DNS code that solves the nonlinear Navier-Stokes equations subject to the Boussinesq approximation in a Cartesian domain to explore the dependence of these dynamics and



effects for various environmental parameters. A LES extension of the DNS modeling capability allowing application to a higher Reynolds number was also employed to explore the nature and implications of radar backscatter from KHI structures in the atmosphere [Franke et al., 2011; Fritts et al., 2011, 2012]. Here we summarize these methods and illustrate some of the results that are pertinent to our application to KHI dynamics observed in NLC images.

We assume a mean flow having an initial horizontal motion given by

$$U(z, t = 0) = U_0 \tanh(z/h)$$
(1)

where U_0 and h are the velocity and depth scales of an assumed unstable shear layer, an initial buoyancy frequency, N, that is constant with altitude, and a minimum initial Richardson number, $Ri = N^2/(|dU/dz|_{max})^2 = N^2h^2/U_0^2 < \frac{1}{4}$ in order to allow KHI development.

Nondimensionalizing with respect to the length, time, and velocity scales h, the buoyancy period, $T_b = 2\pi/N$, and U_0 , the Navier-Stokes equations may be written as

$$\partial u/\partial t + \mathbf{u} \cdot \nabla u = -\nabla p + Ri\theta \mathbf{z} + Re^{-1}\nabla^2 \mathbf{u}$$
 (2)

$$\partial \theta / \partial t + \mathbf{u} \cdot \nabla \theta = (PrRe)^{-1} \nabla^2 \theta$$
 (3)

$$\nabla \cdot \mathbf{u} = 0$$
 (4)

Here $\mathbf{u}=(u,v,w)$ is the velocity vector, p is pressure, θ is potential temperature, and $Pr=v/\kappa$ is the Prandtl number. We assume a Reynolds number $Re=U_0h/v=\lambda_{\mathrm{KH}}^2/(8\pi Ri^{1/2}T_bv)$, with v the kinematic viscosity and λ_{KH} the KH billow wavelength, that is sufficiently large to enable vigorous KHI and secondary instabilities leading to turbulence (Re from 2500 to 10,000) based on our previous studies. $Re\sim2,000,\,8,000,\,\mathrm{and}\,32,000$ are representative of KHI at NLC altitudes having $Ri\sim0.1,\,T_b\sim400\,\mathrm{s},\,v\sim1\,\mathrm{m^2\,s^{-1}},\,\mathrm{and}\,\lambda_{\mathrm{KH}}\sim2.5,\,5,\,\mathrm{and}\,10\,\mathrm{km}$. KHI having smaller Ri or T_b , or larger λ_{KH} , will have correspondingly larger Re. Our DNS and LES to date indicate that higher Re (10,000 compared to 2,500) yield similar KH billow dynamics, but more rapid secondary instabilities as well as differences in secondary instability scales and orientations [e.g., $Fritts\ et\ al.,\,2003,\,2012;\,Werne\ et\ al.,\,2005]$ that will be discussed further below.

We assume Pr=1 to yield uniform resolution requirements in the velocity and potential temperature fields. DNS and LES are performed in domains having dimensions (X,Y,Z)=(4,2,2) and (1,0.33,2) λ_h , respectively, KHI is initiated with the most unstable eigenmode having an amplitude of 0.07 of the maximum initial mean vorticity, and three-dimensional (3-D) modes are initiated with a Kolmogorov noise spectrum with a vorticity amplitude of 0.014.

2.2. Representation of NLC Responses

For our purposes here, we assume that KHI dynamics occur on sufficiently rapid time scales that NLC particle sizes and brightness are not impacted, thus allowing NLC brightness to be assigned as a passive tracer in the initial flow. This allows us to parameterize NLC brightness as a function of the background θ , which is assumed linear with altitude and enables NLC brightness to be written as

$$B(z) = B_0 \exp\left[-(z - z_{\text{NLC}})^2 / 2\sigma_z^2\right] = B_0 \exp\left[-(\theta - \theta_{\text{NLC}})^2 / 2\sigma_\theta^2\right]$$
 (5)

where $z_{\rm NLC}$ and $\theta_{\rm NLC}$ are NLC altitude relative to the maximum wind shear and the potential temperature at the peak of NLC brightness and $\sigma_z = z_{\rm FWHM}/2(2 \ln 2)^{1/2}$ corresponds to an NLC layer having a typical full width at half maximum (FWHM) brightness of $z_{\rm FWHM}$ ~1 km based on the lidar data discussed by BF14, though $z_{\rm FWHM}$ may vary for different events.

3. KHI and Secondary Instability Structures for Representative Ri

We expect KHI at $Ri \sim 0.05$ to 0.20 and sufficiently high Re to approximate the strongest and weakest events that arise on short time scales in stratified environments in the MLT. Hence, we employ evolutions for Ri = 0.05, 0.10, and 0.20 as examples of the range of dynamics we expect to occur near the NLC layer. Examples of these flow evolutions for Re = 2500 [e.g., Fritts et al., 2003; Werne et al., 2005] are shown at 0.5 T_b intervals in Figures 1–3 following attainment of finite-amplitude secondary instability in each case. Images for Ri = 0.05 and 0.10 in Figures 1a, 1b, 2a, and 2b span only 1 T_b because the transition to turbulence is relatively

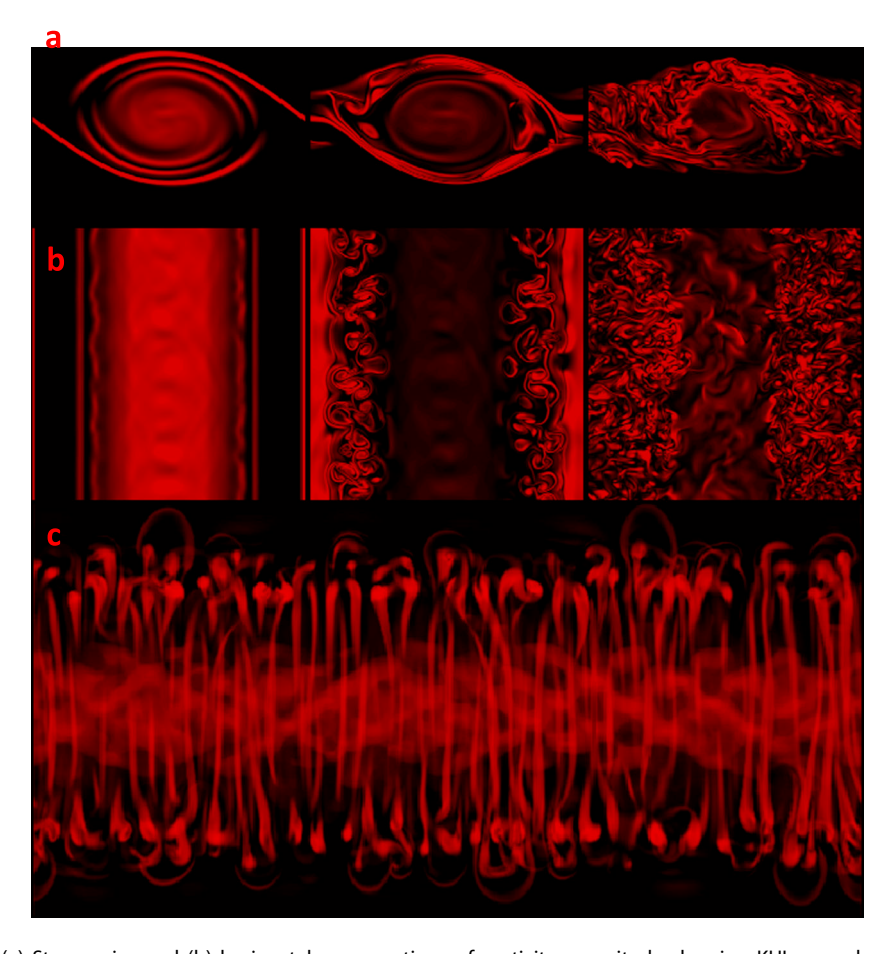


Figure 1. (a) Streamwise and (b) horizontal cross sections of vorticity magnitude showing KHI secondary instability and turbulence evolution at 0.5 T_b intervals beginning at a time of initial finite-amplitude secondary instabilities from a DNS for Ri = 0.05 and Re = 2500 having streamwise and spanwise domain dimensions of λ_{KH} . (c) Horizontal volumetric 3-D view of secondary instabilities at a time near their maximum coherent responses for a spanwise domain width of 2 λ_{KH} (left to right).

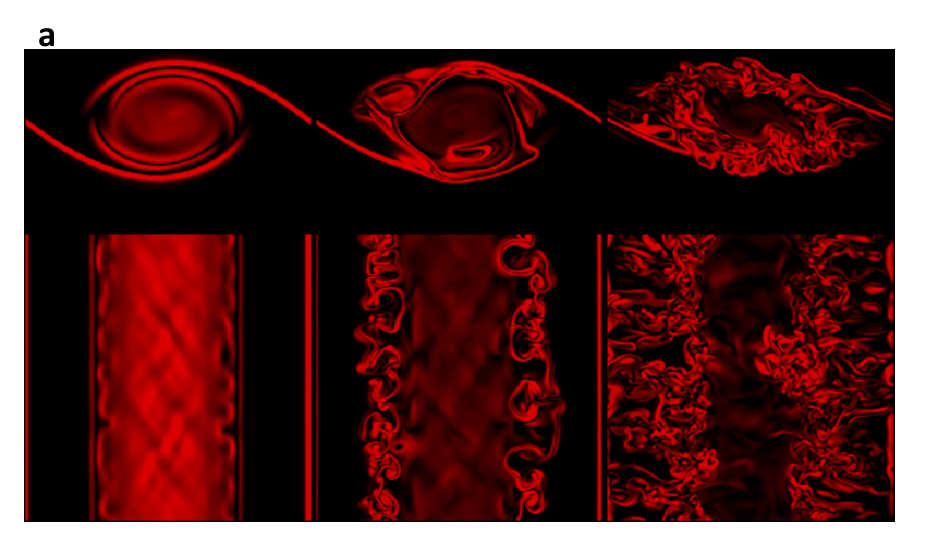


Figure 2. As in Figures 1a and 1b for Ri = 0.10 and Re = 2500.

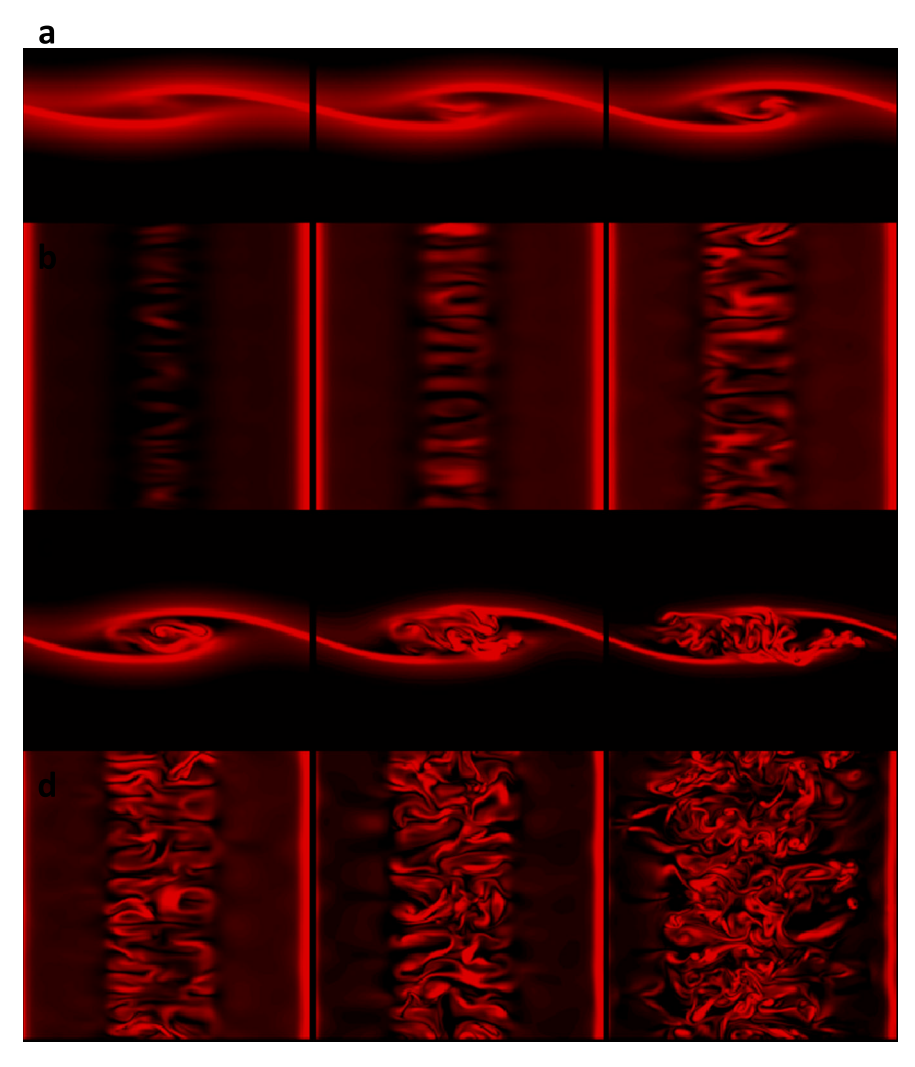


Figure 3. As in Figures 1a and 1b for Ri = 0.20 and Re = 2500 at 0.5 T_b intervals.

rapid at these Ri. Those for Ri = 0.20 span 2.5 T_b due to the slower evolution of instabilities and turbulence in a weaker shear flow. Shown in each case are streamwise-vertical (hereafter streamwise) and horizontal cross sections of vorticity magnitude through the center of the KH billow (billow rotation is counterclockwise). The horizontal cross sections have a spanwise width of $\lambda_{\rm KH}$ in each case.

The time series displayed in Figures 1–3 reveal a strong dependence on Ri of primary KH instability character, secondary instability location and character, and turbulence evolution and intensity. The strongest initial shear flow for Ri = 0.05 is seen to yield deep and broad (streamwise) KH billows (a ratio of maximum billow depth to horizontal wavelength of ~0.5), and large-scale and larger-amplitude secondary instabilities that arise initially in the outer portions of the KH billow (see the left and middle images in Figures 1a and 1b). A volumetric view of the vorticity structures seen from above at a time of large and coherent secondary instabilities is shown in Figure 1c (with the streamwise direction from top to bottom in this image). This emphasizes the approximate streamwise alignment and extent of these instabilities at early times. Secondary instability dynamics for Ri = 0.05 also yield more intense turbulence and more rapid billow breakdown following turbulence generation, compared to the cases with larger Ri. The weakest initial shear flow for Ri = 0.20 (Figure 3) yields shallow billows (a ratio of depth to wavelength of ~0.15–0.2), a more gradual evolution (note the longer interval displayed), much weaker instabilities that arise in the KH billow cores, and turbulence that expands outward throughout the billows with time. The case with Ri = 0.10 (Figure 2) is seen to have a KH billow that is shallower and less extended streamwise than for Ri = 0.05, but is much deeper, with stronger instabilities, than for Ri = 0.20. Comparing Figures 1 and 2, we see that the transition to turbulence is faster for Ri = 0.05 than for Ri = 0.10.

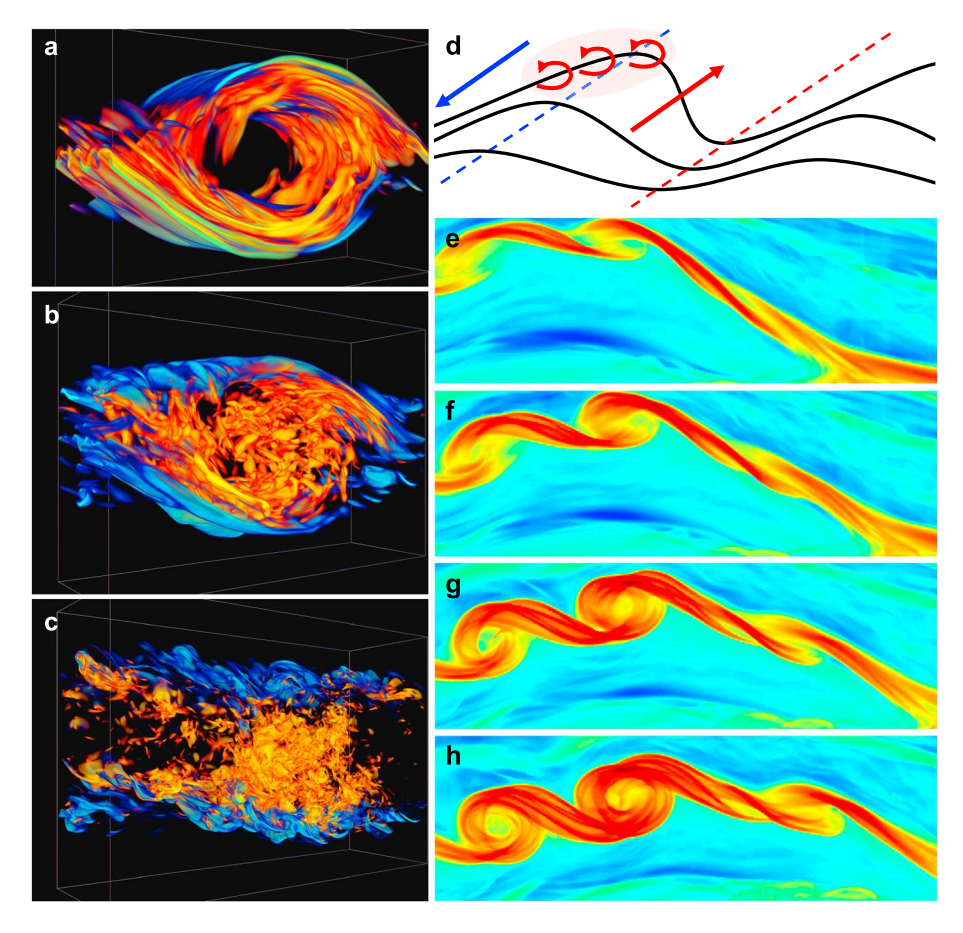


Figure 4. (a–c) Volumetric 3-D views of ε and $Ri\chi$ (red/yellow and blue, respectively) spanning ~2 T_B intervals from a time of maximum coherent secondary instabilities to approximate horizontal homogenization of the turbulent shear layer. As in Figure 1, results are from a DNS for Ri = 0.05 and Re = 2500. Views are from the side and 45° ahead of the KH billow axis relative to the mean wind above the shear layer [Fritts et al., 2003]. (d) Schematic of the anticipated KHI location within the GW field for Event 1. Black lines are surfaces of constant θ and vectors show GW velocities in opposite phases of the wave. (e-h) Time series of KH billows initiated approaching the peak upward displacement due to local GWs (from a multiscale DNS following Fritts et al. [2013]).

Secondary instability structures for Ri = 0.05 [after Fritts et al., 2003] are shown in Figures 4a-4c with 3-D volumetric views of the mechanical and thermal energy dissipation rates at 3 times from initial, large-amplitude structures confined to the billow exterior through billow breakdown and quasi-homogenization of the turbulent shear layer. The panels show these structures from the side and ahead (downstream) of the billow core, relative to the mean flow above the billow. The spanwise extent of the domain for these images is $0.67 \lambda_{KH}$. Figures 4a and 4b correspond approximately to the middle and right images in Figure 1a. These views (Figures 4a to 4c) are also approximately the same perspective as inferred for Event 1 of BF14, which is discussed further in section 4.1 below. These illustrate the initial alignments of the secondary instabilities seen in Figure 1 along the intensified vorticity sheets and the evolution toward more nearly isotropic turbulence structures at smaller scales thereafter. Corresponding 3-D structures can be inferred for Ri = 0.10 from the similar vorticity features in the cross sections in Figure 2 compared to those in Figure 1.

The secondary instability evolution for Ri = 0.20 differs dramatically from those for Ri = 0.05 and 0.10. Referring to Figure 3, we see that secondary instabilities for Ri = 0.20 arise initially in the billow core, have largely streamwise initial alignments, and expand horizontally and vertically to occupy the billow over $>2.5 T_{bi}$ in contrast to the $\sim T_b$ required at Ri = 0.05 and 0.10. At later stages in this evolution, the regions of strong vorticity at the outer edges of these billows also exhibit instabilities preferentially at the leading edges of the regions of inflow into the billow core (see the right images in Figures 3c and 3d). These comprise vortex structures of narrow spanwise extent that include vortex loops at their leading edges.

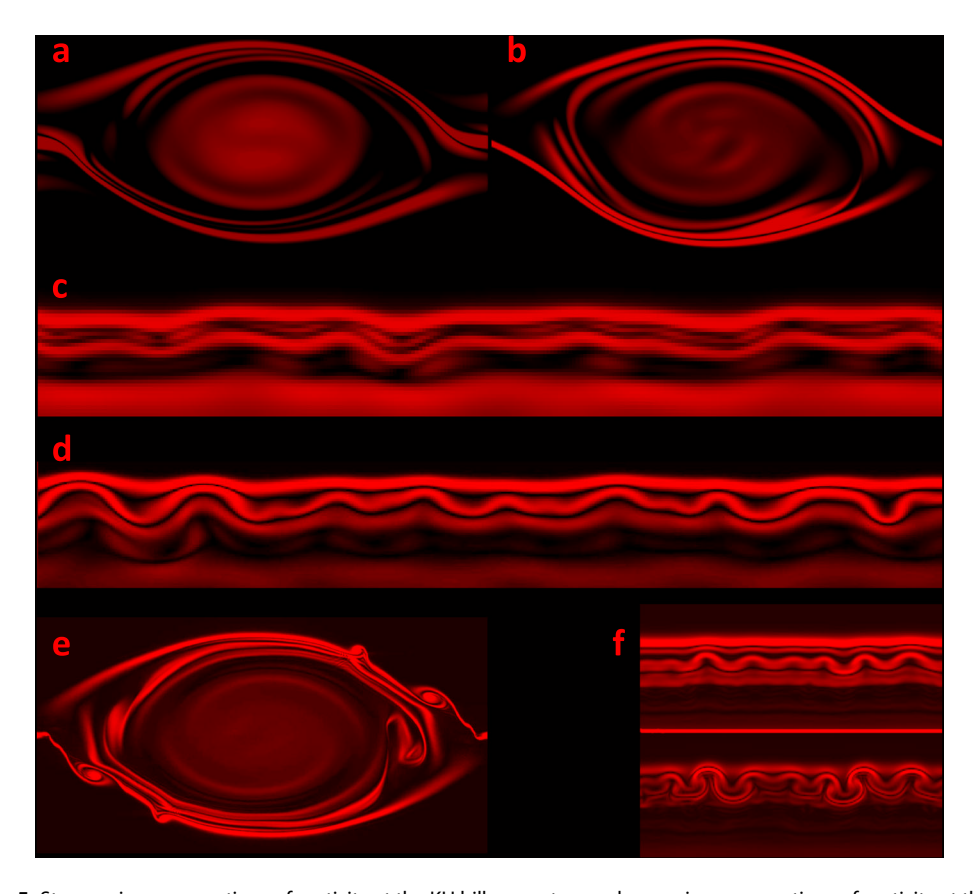


Figure 5. Streamwise cross sections of vorticity at the KH billow centers and spanwise cross sections of vorticity at the top center of the KH billows at a time of finite-amplitude secondary instability for Ri = 0.05 and Re = (a and c) 1,000, (b and d) 2,500, and (e and f) 10,000. The Re = 1000 and 2500 results are from DNS; the Re = 10,000 results are from the LES by *Fritts et al.* [2012]. Note that the spanwise cross sections have spanwise width of 1 λ_{KH} for Re = 1,000 and 2,500 and 0.33 λ_{KH} for Re = 10,000.

To illustrate the influences of Re on KHI dynamics for Ri = 0.05, we employ DNS at Re = 1000 and 2500 and a LES at Re = 10,000 to describe these dynamics for the same initial parameters. The LES code employed for the Re = 10,000 simulation was benchmarked against the DNS code and yielded essentially identical results for Ri = 0.05 and Re = 2500. The KH billows and secondary instability spanwise structures are shown in Figure 5 with streamwise and spanwise-vertical (hereafter spanwise) cross sections, respectively, at times having similar secondary instability displacements at the tops of the billows. The spanwise extents of the computational domains for Re = 1,000 and 2,500 are 1 $\lambda_{\rm KH}$; that for Re = 10,000 is 0.33 $\lambda_{\rm KH}$.

Comparing first the streamwise cross sections in Figure 5, we see that each simulation yields a comparable KH billow depth at maximum billow amplitude, but that vorticity magnitudes and gradients increase at higher Re. The differing vorticity fields are seen in the spanwise cross sections at the billow tops for each Re to yield very different spanwise instability scales. These variations for Ri = 0.05 and Re = 2500 are consistent with the streamwise cross sections displayed in Figure 1b. Secondary instability wavelengths vary from $\lambda_{SI} \sim \lambda_{KH}/7$ for Re = 1,000 to $\lambda_{SI} \sim \lambda_{KH}/9$ and $\sim \lambda_{KH}/21$ for Re = 2,500 and 10,000, suggesting that the secondary instability spanwise scale varies approximately as $\lambda_{SI} \sim Re^{-1/2}$ for Ri = 0.05. Similar variations with Re are expected for Ri = 0.10, given the similarities in secondary instability structures for both Ri.

Finally, recent DNS of gravity wave-fine structure (GW-FS) interactions [Fritts et al., 2013] reveal that KHIs play major roles in such flows. Specifically, deep KHI is preferentially initiated accompanying the maximum upward displacements due to small-scale GW activity. The maximum upward GW displacements accompany the strongest horizontal divergence and vertical convergence within the GW, yielding the most rapidly thinning and intensifying shears of any embedded fine structure. A schematic of the GW displacements implied by the NLC measurements was shown by BF14 in the discussion of Event 1. A slope of the NLC layer



along the GW propagation direction of φ ~15° was inferred from the approximate alignment of the NLC layer with the camera field-of-view (FOV) of ~11° computed by BF14 (see section 4.1 below for further details of the GW field).

The expected occurrence of KHI in such an environment based on a GW-FS DNS parallel to that by *Fritts and Wang* [2013], but having a stronger "turbulent" noise seed more appropriate for the MLT, is illustrated in Figure 4d. The evolution of this KHI event spanning 0.3 T_b in this DNS is shown in the thermal energy dissipation rate field in Figures 4e–4h. We believe that this modeling study closely approximates the KHI response to the underlying GW dynamics observed by BF14. As noted above, observational evidence for such events includes lidar and radar measurements of KH billow structures and apparent turbulent backscatter enhancements in the billow braids that appear to arise at a maximum upward displacement and descend with time thereafter [e.g., Lehmacher et al., 2007; *Pfrommer et al.*, 2009; *Eaton et al.*, 1995].

4. Assessments of KHI and Environmental Parameters in NLC Images

4.1. Event 1: Deep KHI Observed on 24 June 2009

The deep KHI event on 24 June 2009 described by BF14 (Event 1) was apparently initiated by small-scale, superposed GWs having horizontal wavelengths of λ_h ~20–30 km. Evidence of these GW motions, their spatial scales, and their superposition are provided in the projected NLC images (see Figure 4 of BF14). Specifically, superposition and local GW amplitude maxima are revealed by the localized (along the propagation direction) and intermittent (along the GW phases) character of the observed GW field.

These GWs likely induced relatively large vertical displacements, given the strong NLC line-of-sight (LOS) brightness variations at an angle of ~11° from the horizontal at the ~580 km viewing distance inferred by BF14. These strong, thin brightness maxima suggest close alignment of the NLC layer along the LOS at several GW phases, indicating phase slopes of this magnitude or greater in specific regions of the GW field. Assuming the NLC layer was inclined along the LOS, the slope of the GW modulation of the NLC layer along the propagation direction would have been ~15°, (see BF14, Figure 6). The intrinsic and buoyancy frequencies were likely $\omega_i = k_h c_i = 2\pi c_i/\lambda_h \sim 0.01 \, \text{s}^{-1}$ and $N \sim 0.017 \, \text{s}^{-1}$, respectively (with $c_i \sim 30 \, \text{m s}^{-1}$, $\lambda_h \sim 20 \, \text{km}$, and dT/dz $\sim -5.5 \, \text{K/km}$) based on mean temperature profiles at ~83 km [e.g., *Rapp et al.*, 2004]. These values yield $\omega_i/N \sim 0.59$, a GW $\lambda_z \sim 14.5 \, \text{km}$, and a maximum vertical displacement of the NLC layer by the GW of $\zeta' \sim 2 \, \text{km}$, given that parcel motions are inclined along the GW phase structure. Note that estimates of maximum phase slopes depend strongly on the direction of GW propagation, the LOS view, and GW amplitude for larger amplitudes.

The estimate of the GW $\zeta'\sim 2$ km yields a GW vertical velocity of $w'\sim \omega_i\zeta'\sim 20\,\mathrm{m~s^{-1}}$, a GW horizontal velocity of $u_h'\sim (\mathrm{m/k_h})w'\sim 27\,\mathrm{m~s^{-1}}$, and a nondimensional GW amplitude $a=u_h'/c_i\sim 0.9$. This amplitude is likely sufficiently large to enable direct GW "breaking" with sufficient time, based on DNS performed by *Fritts et al.* [2009a, 2009b]. However, the GW appears instead to initiate vigorous and deep KHI, likely because of the contributions of significant mean shears to small values of *Ri.* This is implied by the observed NLC advection and KH billow rotation during this event, which reveal significantly stronger westward motions above than below the KH billows. These dynamics also closely resemble those modeled by *Fritts and Wang* [2013] displayed in Figures 4e–4h.

We now turn to the KHI dynamics that occur within the perturbed GW environment. These dynamics are displayed in Figure 5 of BF14, a subset of which, spanning 5 min (from 22:55 to 23:00 UT), is shown with zoomed views in Figure 6 (left column). This interval spans ~80% of the T_b ~370 s expected for the mean NLC environment. There is uncertainty in the true temperature gradient, however, because the MLT environment is essentially always modulated by GWs, including those discussed above and others at smaller amplitudes and/or lower frequencies that do not yield measureable NLC perturbations in all cases. This imposes uncertainty in the appropriate N (and T_b and Ri) for the observed KHI that will be discussed further below.

We expect the KH billows to be aligned approximately in the plane of GW propagation (~30°E of N) if the shears accompanying the observed GWs dominate the local *Ri*. If there are significant mean shears in addition to those induced by the observed GWs, however (as suggested by the NLC westward drifts noted by BF14), KH billow alignment may depart from the plane of the primary GWs themselves. In this case, the mean shears likely cause the plane of KHI to be more nearly zonal than meridional. Independent of their orientation, the KH billows appear to arise upstream and accompanying an expected bright, descending GW phase

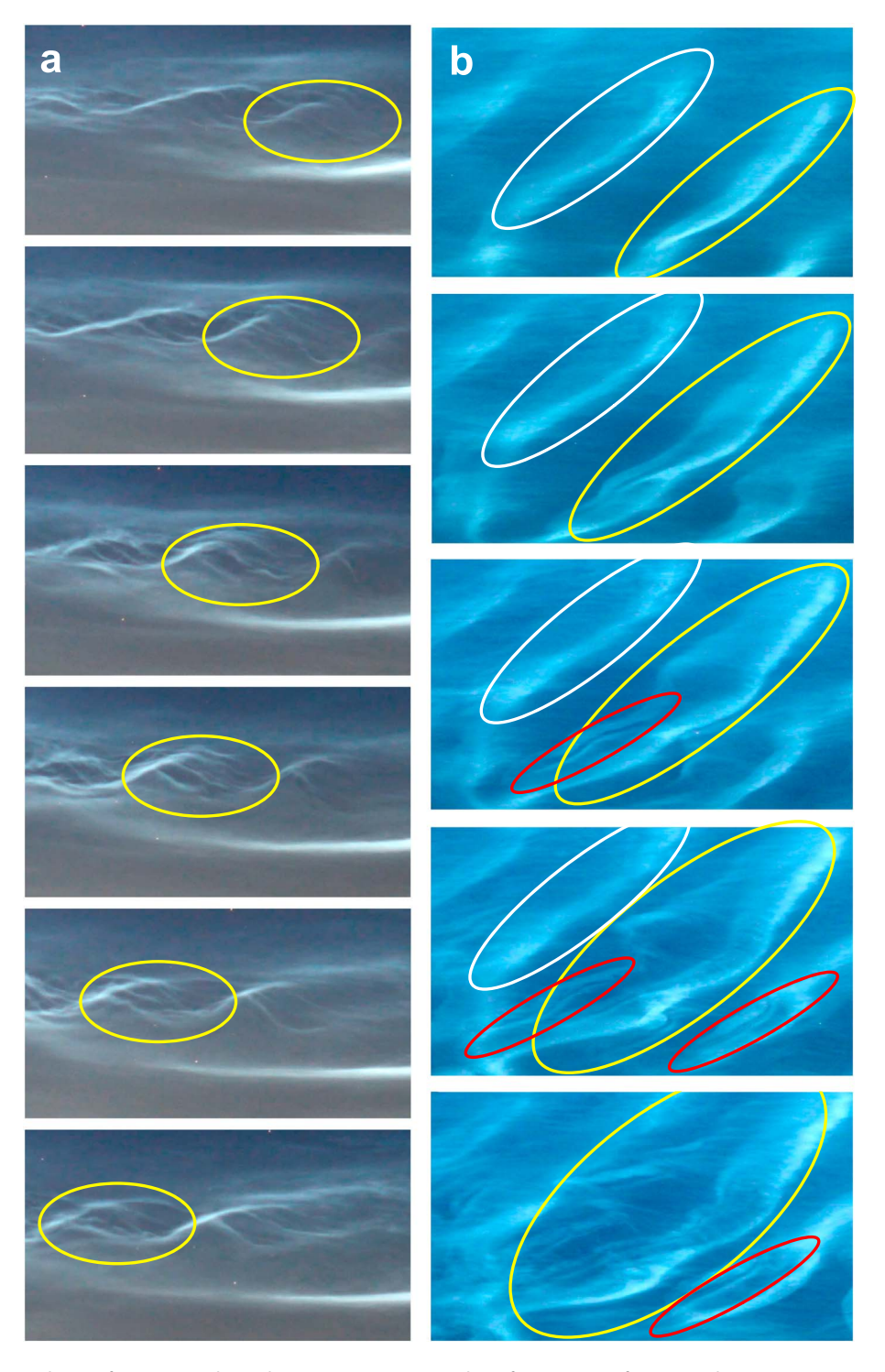


Figure 6. Subsets of KH images shown by BF14 at 1 min intervals (a) from Figure 5 for Event 1 beginning at 22:55 UT and (b) from Figure 8 for Event 2 beginning at 22:59 UT. The fields extend approximately 20 and 10 km east-west (left to right) for Events 1 and 2, respectively. Yellow ovals in Figure 6a highlight the evolution in one billow over this interval. White and yellow ovals in Figure 6b highlight relatively undisturbed and highly disturbed KH billow cores, respectively. Red ovals in Figure 6b illustrate small-scale features that show the capabilities of the method that have not yet been simulated in our KHI modeling.

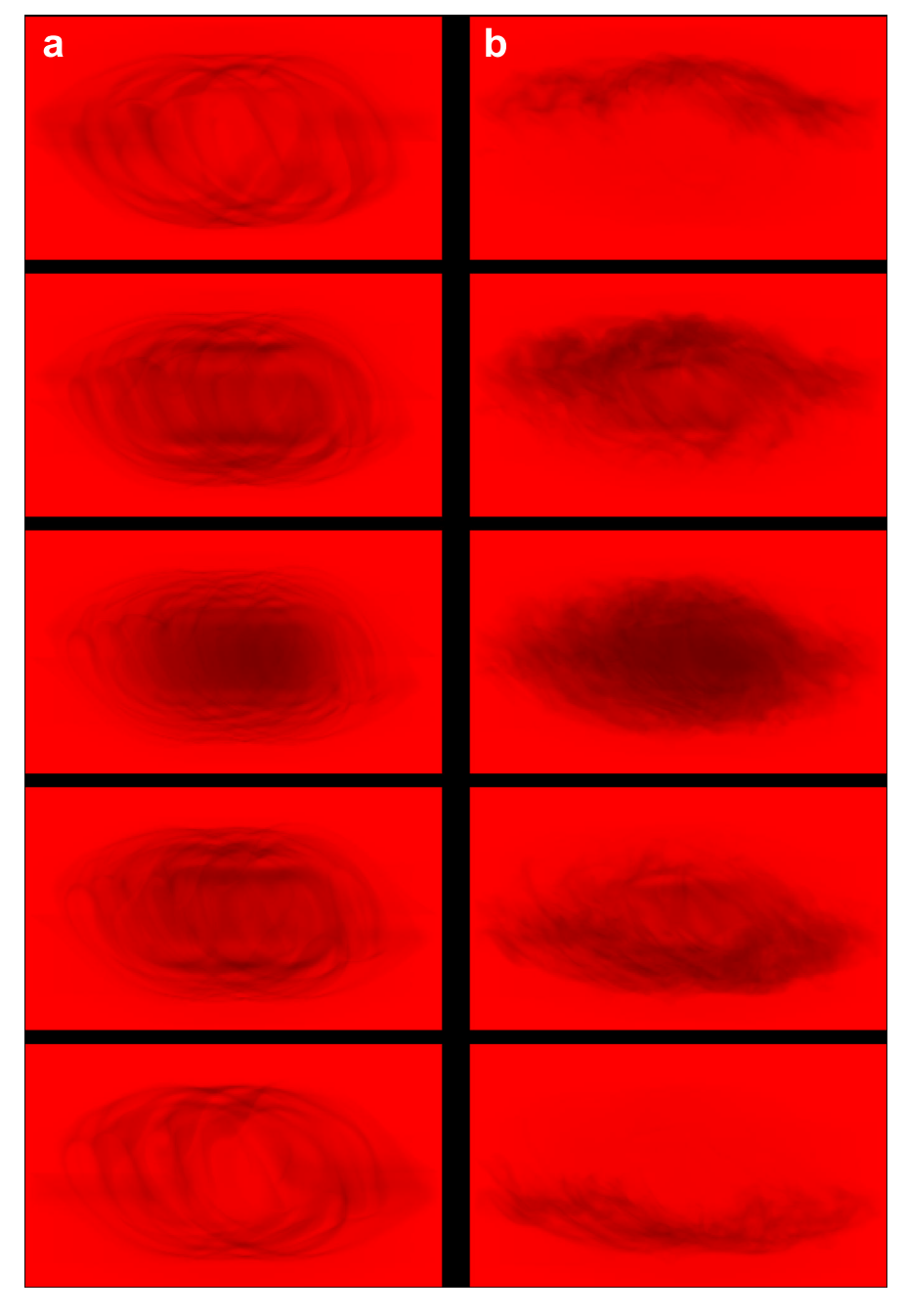


Figure 7. Modeled variations of NLC brightness for a KH billow having Ri = 0.05 and Re = 2500 at (a) t = 0.4 T_b and (b) t = 0.8 T_b after the first image in Figure 1 with NLC altitudes at 1, 0.5, 0, -0.5, and -1 km (top to bottom) relative to the maximum initial shear. One KH billow having streamwise and spanwise extent of 1 λ_{KH} exhibits NLC brightness in each panel.

following the coherent, stable, and bright upstream phase aligned with the LOS seen at lower right in each image of Figure 6. Whether the KH billows are aligned in the GW propagation plane, or more nearly zonally, they will appear to occur at shorter wavelengths than in reality (by up to ~1.5 times). They will also appear to remain at the same altitude as they evolve, because our FOV is largely along the GW phase surface at the KHI location. This latter effect would make the billows appear to be aligned in the zonal direction rather than in the plane of GW propagation for the same reason that viewing along the GW phase structure yields NLC brightness maxima. Alternatively, if the KH billows are aligned more nearly zonally, given apparent zonal shears, they would have wavelengths more nearly comparable to those seen in the NLC observations described by BF14. Given their initiation by, and location relative to, the GW field, and the appearance of



secondary instabilities within the KH billows at displaced positions horizontally however, it appears more likely that both GW and mean shears contribute and that the KH billows cannot be aligned strictly zonally.

Thus, there are two apparent limits for the true KHI wavelengths implied by the observations by BF14 and the discussion above. Alignment along the GW propagation plane (\sim 30–40°E of N) implies λ_{KH} \sim 10 km. Alternatively, alignment at an intermediate angle due to possibly important zonal wind shears would yield a true λ_{KH} \sim 8 km. Given the estimated depths of the observed initial KH billows in Event 1 of \sim 2.5 to 3 km and their likely wavelength range of \sim 8–10 km, the most likely ratios of billow depth to wavelength vary in the range \sim 0.25–0.4, with a most likely estimate (assuming an orientation between the plane of GW propagation and the zonal direction) of \sim 0.35–0.4. Laboratory and numerical studies indicate that these ratios correspond to initial Ri of \sim 0.05–0.10 (a larger ratio for smaller Ri), respectively [e.g., *Thorpe*, 1973; *Fritts et al.*, 2003; *Werne et al.*, 2005]. Hence, we employ our DNS and LES performed for Ri = 0.05 and 0.10 in our interpretation of these dynamics.

To evaluate the likely KHI dynamics underlying the features seen in the NLC images in Figure 6 (left column), we employ our KHI DNS having Ri = 0.05 and 0.10 to simulate NLC images for a "most likely" NLC brightness distribution at various altitudes relative to the shear layer responsible for KHI. Experiments with several NLC brightness depths, guided by typical lidar measurements (BF14), led to the choice of a brightness depth of $z_{\rm FWHM} = 1$ km with an assumed $\lambda_{\rm KH} \sim 10$ km. Sensitivity of the NLC signatures of a KH billow for Ri = 0.05 at peak secondary instability and during the turbulent decay phase ($\delta t \sim 0.4~T_b$) for $z_{\rm NLC} = 1, 0.5, 0, -0.5$, and -1 km relative to the shear layer are shown in Figure 7. Here we have assumed that the plane of KHI is aligned at 45°E of N for illustration, with the views in the plane of the NLC layer from 45° ahead (or downstream) of the KH billow relative to the wind above the shear layer. For convenience, this is the approximate viewing geometry inferred by BF14 for Event 1 shown in Figure 6 (left column). Comparisons of these images with the NLC images in Figure 6 (left column) suggest an NLC layer centered $\sim 0.5-1$ km above the shear layer. Hence, additional computed NLC images spanning 1 T_b at intervals of 0.2 T_b beginning at incipient secondary instability for Ri = 0.05 and 0.10 for NLC altitudes of 0.5, 0.75, and 1 km above the shear layer are shown in Figures 8 and 9.

Comparisons of Figures 8 and 9 with the NLC images suggest that both DNS image sequences include features that closely resemble the observed KHI evolution and others that are quantitatively different. The initial transition in the NLC images from an approximately two-dimensional (2-D) KH billow exhibiting very weak secondary instability striations (at right, top panel of column a in Figure 6) to large-amplitude, coherent streamwise secondary instabilities, to thinning of the billow and initial breakdown of the secondary instability structures spans ~5 min. Features that appear common to the observations and model predictions include (1) a maximum ratio of billow depth to $\lambda_{\rm KH}$ of ~0.4 to 0.5 (when corrected for viewing angle), (2) rapid onset and growth of initial secondary instabilities, (3) apparent confinement of these structures to the outer billows, (4) a loss of secondary instability coherence and increase in complexity with time, and (5) thinning and breakdown of the billows thereafter.

Features that appear to differ between the observations and DNS or LES include (1) a longer interval over which the observed secondary instabilities evolve compared to the DNS at Re = 2,500 (or the LES for Ri = 0.05 at Re = 10,000) and (2) a larger spanwise scale of the secondary instabilities than predicted for Ri = 0.05 (and anticipated for Ri = 0.10) at Re = 10,000. We note, however, that the secondary instability spanwise scales seen in Figures 8 and 9 are larger than the initial scales observed to arise in Figures 1 and 2 but are comparable to the scales seen in middle panels Figures 1b and 2b, and in the middle and right panels of each row in Figures 8 and 9. This is because larger-scale secondary instabilities preferentially attain larger amplitudes and dominate the finite-amplitude secondary instability responses. These modeled NLC secondary instability scales appear to be comparable to those seen in the NLC images.

The areas of agreement between the KHI observations and modeling provide strong evidence for an initial KHI $Ri \sim 0.05$ to 0.10 needed to achieve deep billows, rapid secondary instability onset and growth, and initial confinement of these structures to the outer billows. Specifically, there are no features of the observed KHI evolution suggesting Ri > 0.10. However, the longer observed KHI evolution time scale and the larger observed secondary instability spanwise scales are strong evidence for an effective turbulent Reynolds number of $Re_{\text{turb}} = U_0 h/v_{\text{turb}} \sim 2500$ or less for the inferred range of Ri. Given $Re = U_0 h/v = \lambda_{\text{KH}}^2/(8\pi Ri^{1/2}T_bv)$ as defined above, the observed KHI scales, our inference of $Ri \sim 0.05$ to 0.10 for the observed KHI and the environmental parameters, U_0 , h, T_b , and v inferred above, we obtain ranges of expected $Re \sim 16,000$ to 32,000 for Ri = 0.10 and $Re \sim 22,000$ to 44,000 for Ri = 0.05.

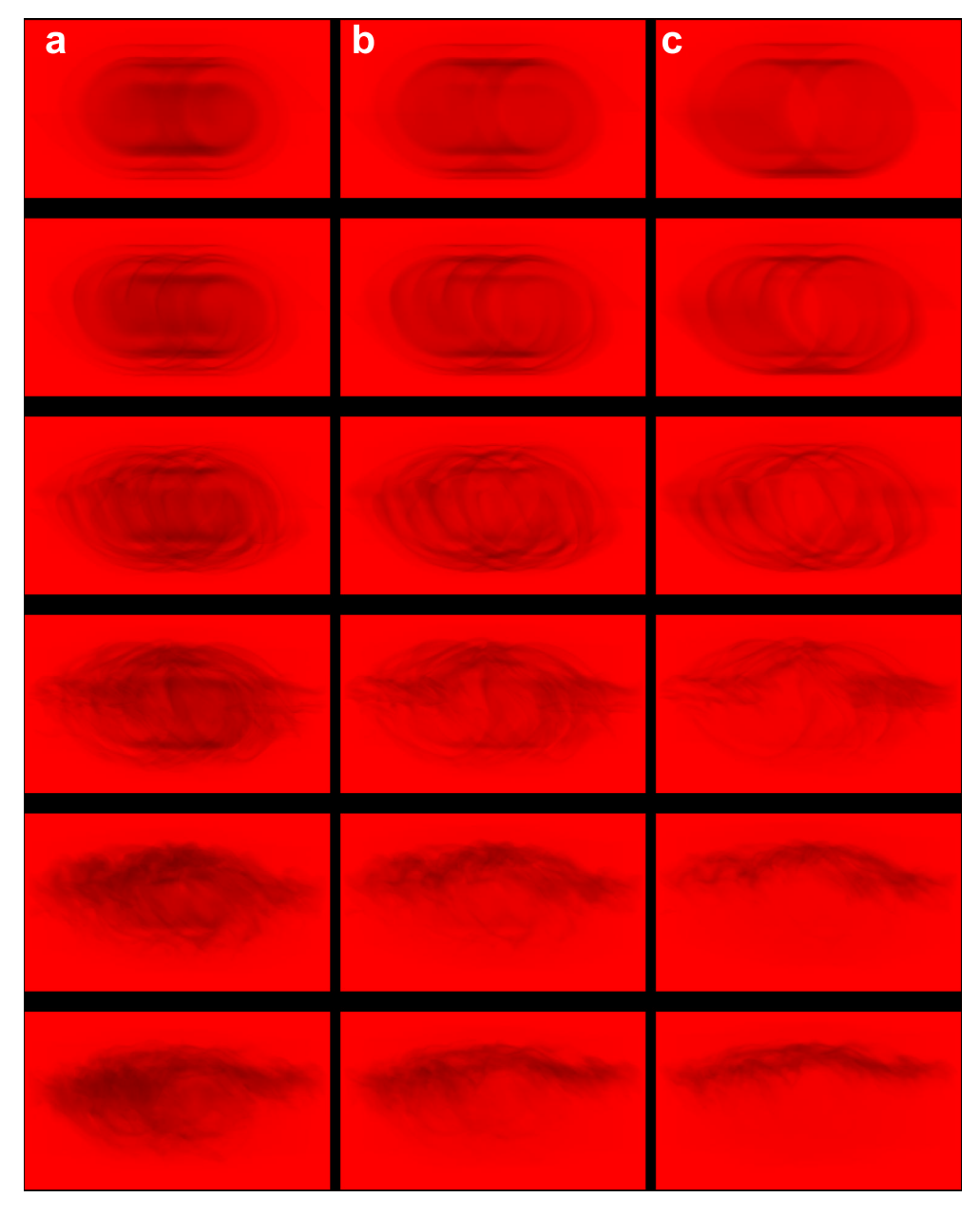


Figure 8. As in Figure 7 for Ri = 0.05 at NLC altitudes relative to the initial shear layer of (a–c) 0.5, 0.75, and 1 km above the maximum initial shear spanning a buoyancy period at intervals of 0.2 T_b (top to bottom).

By comparison, the observed secondary instability spanwise scales seen in the NLC images of Figure 6 ($\lambda_{\rm Sl} \sim \lambda_{\rm KH}/5$ for $Ri \sim 0.05$ to 0.10), the more gradual evolution and decay of secondary instability, and $Re \sim \lambda_{\rm Sl}^{-2}$ inferred above, imply $Re_{\rm turb} \sim 500$ to 1000 for this event. In summary, the inferred Re is $\sim 20-40$ times smaller than $Re = U_0 h/v$ for this KHI event, implying a turbulent $Re_{\rm turb} = U_0 h/v_{\rm turb} \sim 20-40$ Re and an effective turbulent viscosity of $v_{\rm turb} \sim 20-40$ v or $\sim 10-20$ m² s⁻¹ at NLC altitudes. If this is a realistic and representative value of $v_{\rm turb}$ it places a strong constraint on the minimum KHI scales that can lead to turbulence. For example, this $v_{\rm turb}$ implies that KHI having $\lambda_{\rm KH} < \sim 3-5$ km (hence $Re_{\rm turb} \sim 100-250$ at NLC altitudes) will either remain laminar or lead to very weak secondary instability and turbulence, despite having much larger apparent Re based on v.

These estimates are, of course, dependent on the assumptions, inferences, and modeling of KHI and environmental parameters discussed above. Different parameters will change these results quantitatively, but not qualitatively. The inevitable result is that the observations by BF14 of KHI dynamics impacting the NLC layer in Event 1 imply a

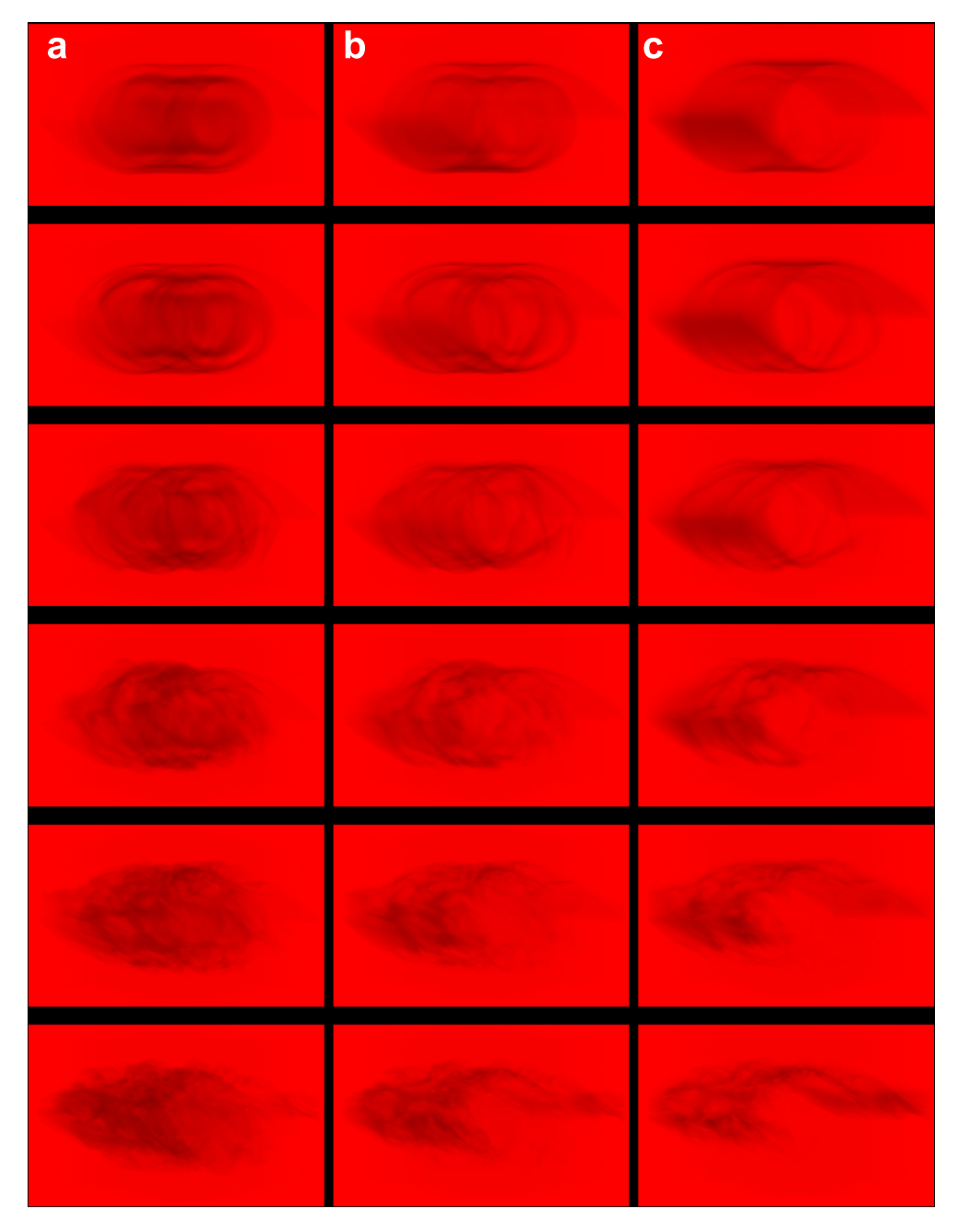


Figure 9. As in Figure 8 for Ri = 0.10.

turbulent (or "eddy") viscosity, $v_{turb'}$ accompanying background (preexisting) turbulence from previous instability and turbulent events that is an order of magnitude or more larger than v at this altitude. Indeed, the inferred ratio of turbulent to kinematic viscosity, $v_{turb}/v \sim 20$ –40, is in surprisingly good agreement with the typical range of ε and v_{turb} inferred with high-resolution in situ probes at these altitudes in the polar summer mesosphere [e.g., $L\ddot{u}bken$ et al., 1993, 2002; $L\ddot{u}bken$, 1997]. These results also imply an enhanced level of turbulent or eddy diffusion and corresponding implications for other dynamics, such as GW breaking and multi-scale superpositions that we expect to also be strongly dependent on Re_{turb} . Additional discussion of these implications is provided in section 5 below.

4.2. Event 2: Shallow KHI Observed on 1 August 2009

The large-scale flow occurring on 1 August 2009 described by BF14 differs dramatically from that discussed for Event 1 above. Whereas large-amplitude, small-scale GWs are largely responsible for the KHI character in



Event 1, Event 2 occurs without obvious, strong GW perturbations of the NLC layer, except perhaps on much larger spatial scales and/or at smaller amplitudes (see Figure 7 of BF14). Event 2 also occurs closer to the viewing location than Event 1 (a range of ~280 km viewing to the north); hence, the view is somewhat more from below than in Event 1. Referring to the subset of Event 2 shown at right in Figure 6 (having image widths of 10 km), we see generally parallel apparent KHI structures having dominant horizontal wavelengths λ_{KH} ~4–5 km (primarily north-south phases) over a large region, given that the off-zenith viewing angle of ~70° implies an apparent shortening of north-south distances by ~3 times. There are nevertheless significant along-phase undulations and variable intensities that lead to distinct differences in KHI evolution at later times. These likely have roots in variable initial conditions (e.g., shear structure, modulations by GWs, or optimal KH wavelengths and growth rates) prior, or subsequent, to KHI initiation. The modulated KHI intensities yield differential billow core rotation rates (see especially the yellow image highlight at right in Figure 6) and apparent splitting of the more modulated billow cores as they intensify.

In contrast to the KHI characteristics seen in Event 1, there is no evidence in Event 2 of streamwise-aligned secondary instabilities seen to arise in our DNS and LES at $Ri \sim 0.05$ and 0.10. Instead, this time series exhibits what appears to be a slow evolution of relatively weak, narrow KH billow cores spanning ~ 10 min in Figure 8 of BF14 and 4 min in the subset image sequence at right in Figure 6. Secondary instabilities and turbulence appear to arise in, and be confined to, the billow cores at early stages, as seen in the DNS for Ri = 0.20 in Figure 3. Most billow cores expand horizontally very slowly (see Figure 8 of BF14 and the core highlighted with white ovals at right in Figure 6). The exception is the split billow core (highlighted with yellow ovals at right in Figure 6), where the new cores evolve somewhat more quickly thereafter.

The KHI in Event 2 evolves much more slowly than that seen in Event 1, presumably because of the weaker initial shears or larger N^2 [e.g., Goldberg et al., 2004] yielding larger initial Ri. We expect this based on the "semicircle" theorem of Miles [1961] and Howard [1961], which constrains the KHI growth rate to $\alpha < k_{KH}c_{im}$, where $k_{KH} = 2\pi/\lambda_{KH}$ and k_{Cim} is the maximum possible imaginary KHI phase speed having a magnitude $k_{Cim} = \Delta U(z)/2$, where $k_{Cim} = \Delta U(z)/2$ is the velocity range for which $k_{Cim} = k_{Cim}/2$ in the plane of the KHI. As will be seen below, this implies a very much slower and less energetic KHI evolution than that seen in Event 1.

To interpret the Event 2 KHI structures more quantitatively, we employ our KHI DNS for Ri = 0.20 to simulate NLC brightness distributions for an NLC layer having several depths and at various separations from the KHI shear layer. Referring to Figure 3, and assuming a KH billow wavelength of 5 km, we expect that an NLC layer having either $z_{\rm FWHM}$ or $|z_{\rm NLC}| > 1$ km will yield weak sensitivity to the shallow KH billow structures for Ri = 0.20. Hence, we consider $z_{\rm FWHM}$ = 0.5 and 1 km and $z_{\rm NLC}$ = 0, 0.5, and 1 km. The results for $z_{\rm FWHM}$ = 0.5 km and $z_{\rm NLC}$ = 0 km appear to provide the closest match to the observed Event 2 NLC evolution, and these are shown at 1 T_b intervals for assumed 70° and 45° off-zenith viewing angles in Figures 10a and 10b. In each case, the computed brightness images span streamwise and spanwise domain widths of 1 $\lambda_{\rm KH}$, respectively. Finally, to be confident that the Ri = 0.20 results are representative for high Ri and weak KHI cases, we performed an additional DNS for Ri = 0.22 (not shown). This revealed a very similar, but slower and weaker, billow evolution that required an additional $\sim T_b$ to exhibit initial secondary instability and mixing.

Referring to Figure 10, we see that the initial brightness maxima accompany the billow cores and have roughly Gaussian streamwise brightness variations extending \sim 0.2 $\lambda_{\rm KH}$, consistent with the streamwise extent of the billow core mixing at the earliest times in Figure 3. Several T_b are required for the weaker billow turbulence in this case to extend throughout the streamwise $\lambda_{\rm KH}$. Indeed, both the vorticity fields indicating the extent of billow turbulence in Figure 3 and the simulated NLC images in Figure 10 suggest an initial doubling of the streamwise extent of the turbulent billow cores spanning \sim 1.5–2 T_b at early stages. This estimate appears to agree reasonably with the slow evolutions of the billow cores spanning only \sim 0.65 T_b at right in Figure 6. Specifically, the billow core highlighted with white ovals exhibits a slow expansion and apparent diffusion of the billow core.

In contrast to the evolution just discussed, the initial billow core highlighted with yellow ovals exhibits a more rapid initial expansion, accompanying apparent splitting of the core and a somewhat more rapid evolution thereafter. Evidence of the onset of these dynamics is seen in the first two images at right in Figure 6. Here the initial billow core clearly exhibits strong twisting, due to differential rotation along the core (e.g., spanwise-varying shear strength, due to local intensification by a GW or other small-scale influence; see Figure 4d).

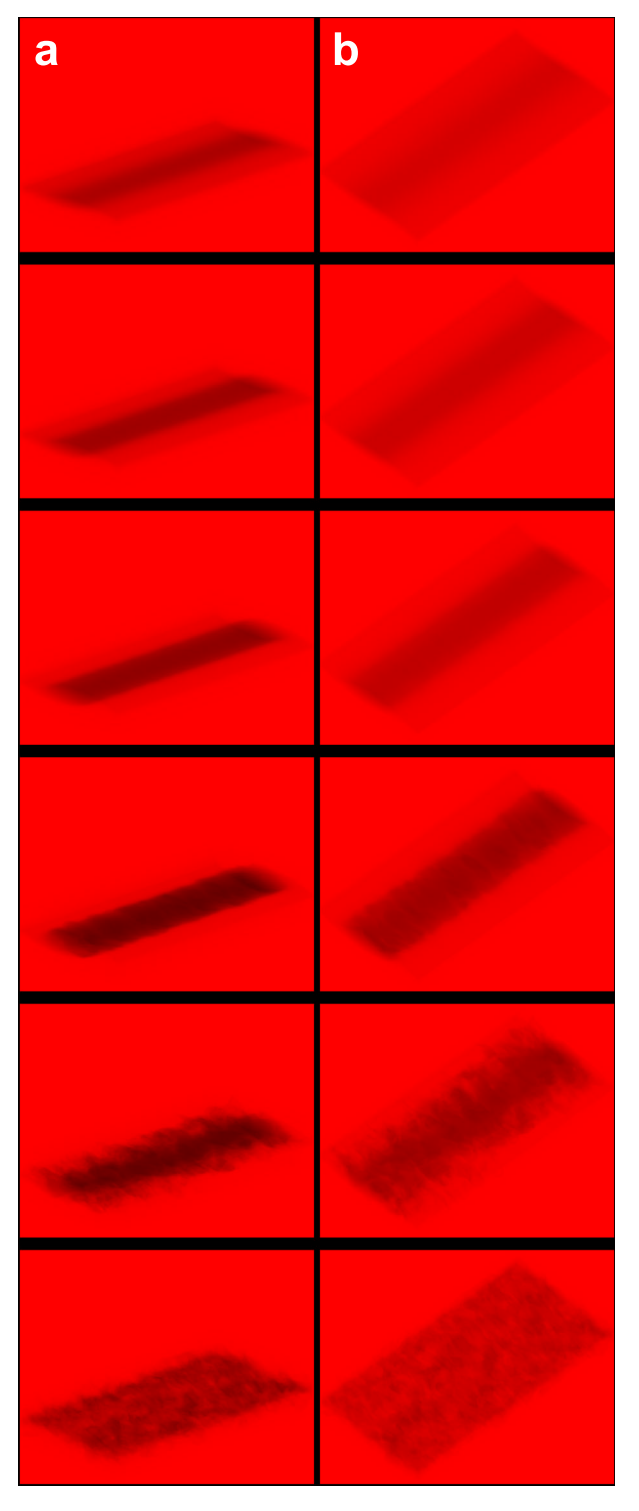


Figure 10. Modeled variations of NLC brightness for a KH billow having Ri = 0.20 and Re = 2500 viewed at (a) 70° and (b) 45° zenith angles at 1 T_b intervals beginning at initial billow rollup. To be consistent with observed scales and brightness variations in Event 2, we assume $\lambda_{\rm KH} = 5$ km, $z_{\rm FWHM} = 0.5$ km, and an NLC layer centered at the maximum initial shear. KHI orientation is assumed to be 45° from the viewing angle. As in Figure 7, one KH billow having streamwise and spanwise extent of 1 $\lambda_{\rm KH}$ exhibits NLC brightness in each panel.

This initiates core splitting and formation of two emerging, intertwined cores, yielding the two distinct cores at later stages. The process is common in vortex interactions accompanying the turbulence cascade to smaller scales. Perturbations leading to breakup of the initial billow core are known as Kelvin "twist waves" [Kelvin, 1880], which have been identified and analyzed in previous numerical simulations of GW breaking [e.g., Andreassen et al., 1998; Fritts et al., 1998, 2003, 2009b] and diagnosed theoretically [e.g., Arendt et al., 1997, 1998]. The subsequent evolution of the separate billow cores is surely influenced by the stable stratification at the larger scales on which the KHI is evolving, in contrast to typically weaker stratification for small-scale vortices interacting within a turbulence field. This KH billow evolution may be the first direct observation of large-scale twist wave dynamics in the MLT. It is also a clear demonstration of the potential for studies employing thin NLC as dynamical tracers.

The apparent initial KH billow and turbulence dynamics observed in Event 2 appear to be in reasonable agreement with the DNS of KHI at Ri = 0.20 and Re = 2500 described above and displayed in Figures 3 and 10, despite the potential for differences in Re and Re_{turb} , or v and v_{turb} , between observations and modeling. Assuming λ_{KH} ~4 km, $T_h \sim 400 \text{ s}$, and only kinematic viscosity, $v \sim 1.5 \text{ m}^2 \text{ s}^{-1}$, the observed KHI has Re ~2500, as simulated. Indeed, the smallscale features seen in Figure 3 and accounting for the apparent fine structure in the simulated NLC images in Figure 10 are not seen in the NLC images at right in Figure 6, despite the very high resolution imagery. This suggests, as in Event 1 above, that the observed billows actually have a somewhat lower Returb than Re, hence a somewhat larger v_{turb} than v, given the much larger apparent spanwise scales of the billow cores at later stages in the evolution.

Summarizing the observed KH billow structures and evolutions in Event 2 and the DNS for Ri = 0.20 displayed in Figure 2, we see good apparent agreement in several areas, including the following: (1) confinement of secondary instability and



turbulence to the billow cores at early times, (2) slow evolutions of initial secondary instability and turbulence extending throughout the KH billows that span \sim 2 T_b or longer in the observations and the DNS, and (3) along-core variations in secondary instability, turbulence strength, and the rate of horizontal turbulence expansion at late stages. Differences between the Event 2 observations and corresponding high-Ri DNS include the following: (1) modulations of the observed initial billow spacing and core rotation intensity that are not present in the DNS, (2) splitting of the billow cores in cases where the observed billows exhibit strong along-core modulation in intensity, (3) more rapid core evolution and spanwise modulation of the more intense cores following splitting, and (4) apparent differences in core fine structure, or lack of, suggesting a lower Re_{turb} than Re for the observed billows compared to the DNS at higher Re.

5. Discussion

We inferred above ratios of $v_{\rm turb}/v \gg 1$ by comparing observed KH billow evolutions in Events 1 and 2 with DNS of the KHI dynamics at $Re \sim 1,000$ to 10,000. For the stronger KHI dynamics in Event 1, this ratio was estimated to be $v_{\rm turb}/v \sim 20-40$. A specific ratio for Event 2 was not inferred, but it is likely significantly smaller than for Event 1, or else the KH billows may have exhibited no secondary instability and turbulence at all. A best guess here might be that a needed $Re_{\rm turb}$ allowing secondary instability and turbulence for $Ri \sim 0.20$ in Event 2 is $Re_{\rm turb} \sim 500$ or greater (also depending on Ri), implying a maximum $v_{\rm turb}/v \sim 5$. This is because KHI secondary instabilities are increasingly suppressed as Ri increases and Re decreases ([Klaassen and Peltier, 1985; Palmer et al., 1994, 1996]; also see Figure 5). These estimates seem roughly consistent given that we should expect stronger background turbulence when the underlying GW and instability dynamics are more energetic.

The inferences of $v_{\rm turb}/v \gg 1$ at NLC altitudes for both of our observed KHI sequences in section 4 have a number of implications for MLT dynamics. These include the following: (1) constraints on the minimum scales of KHI that contribute significantly to turbulence and mixing in the MLT, and likely at lower and higher altitudes. (2) similar constraints on the smallest scales and intensities of other instabilities and turbulence arising from GW breaking and multi-scale interactions. (3) a potential to employ such assessments to characterize variability of $v_{\rm turb}/v$ in space and time, including geographic, seasonal, and interhemispheric variations. (4) a potential to assess $v_{\rm turb}/v$ modulation by planetary waves (PWs) and tides; and (5) a potential to extrapolate these results to lower and higher altitudes, given their expected dependence on GW scales and variances and how these vary in altitude.

We expect that the dynamics accounting for background turbulence levels and the ratio of $v_{\rm turb}/v$ vary roughly as GW kinetic energy and the mechanical energy dissipation rate, ε , thus more slowly with altitude than $1/\rho(z)$, but with enhancements accompanying increasing stability as anticipated by VanZandt and Fritts [1989]. Hence, we expect $v_{\rm turb}/v$ to vary from much larger values near the stratopause, where GW dissipation and momentum deposition begin to have large influences to values ~1 in the lower thermosphere where kinematic viscosity largely suppresses GW and shear flow instabilities. Where previous estimates have been performed, we find surprising agreement. For example, there is rough agreement between our estimate of $v_{\rm turb}/v \sim 20$ –40 under strong GW forcing conditions and those employing estimates of ε and $v_{\rm turb}$ inferred with high-resolution in situ probes in the polar summer mesosphere [e.g., $L\ddot{u}bken$ et al., 1993, 2002; $L\ddot{u}bken$, 1997; Rapp et al., 2004]. Our estimate is also comparable to that by Hecht et al. [2005] employing airglow measurements of a large-scale KHI event.

The identification of vortex twist wave dynamics in Event 2 also implies a potential for additional studies employing NLC observations as a sensitive tracer of such dynamics at scales of ~100 m to 1–2 km. Such observational studies have not been possible previously due to lack of effective "3-D" sensitivity to these small-scale dynamics. Given the strong kinematic and turbulent viscosity constraints on small-scale motions, such measurements offer an enticing ability to characterize transitional GW and shear flow instability dynamics at the minimum spatial scales anticipated to occur at these altitudes.

6. Summary and Conclusions

The companion paper by BF14 described two apparent KHI events observed in NLC near the summer mesopause over Scandinavia employing ground-based cameras at Kühlungsborn, Germany, and Trondheim, Norway. Those observations enabled detailed assessments of the primary KHI dynamics and their accompanying



secondary instabilities, turbulence generation, and KH billow decay. This paper performed high-resolution DNS and LES of KHI dynamics at Ri and Re thought to be representative of the dynamics described by BF14 to interpret those observations more quantitatively. Very reasonable agreement between observed and modeled KHI dynamics was found in each case, lending confidence to our comparisons and to inferences drawn from them. These include the following: (1) demonstration of the value of NLC observations for quantifying small-scale dynamics at MLT altitudes (and to a degree not previously possible) because of the high sensitivity of thin NLC layers to small-scale flow features, as forecast by Witt [1962]; (2) evidence and confirmation of the pervasive, but spatially and temporally intermittent, roles of small-scale GWs and KHI in the dynamics of the MLT; (3) quantification of the roles of GWs in modulating KHI at small spatial scales; (4) demonstration of the ability to provide quantitative estimates of KHI and initial environmental parameters, e.g., the initial Richardson number, Ri, and effective, or turbulent, Reynolds number, Re_{turb} , based on observations of NLC displays; and (5) inference of the effective, or turbulent, viscosity compared to the expected kinematic viscosity, v_{turb}/v , based on the ability to quantify secondary instability structures and scales in NLC observations and compare these with DNS results spanning the range of environmental parameters.

We believe that such coupled observational and modeling capabilities will enable far greater quantification of small-scale GW and instability dynamics than has been possible to date. Assuming this is the case, they will contribute significantly to a more complete statistical characterization of the roles of these dynamics in a number of parameters that require parameterization in large-scale general circulation, weather, and climate models. These include (1) the spatial localization and intermittency of GW dissipation and momentum deposition, (2) the spatial and temporal scales that contribute most to these effects, (3) the induced diffusion and mixing accompanying such events, and (4) the implications of these localized dynamics for evolution of the GW spectrum, and the importance and major scales of secondary GW sources, impacting higher altitudes. Indeed, such NLC observations may offer unique capabilities for understanding small-scale neutral dynamics at high latitudes, as foreseen by Witt [1962] many years ago.

Acknowledgments

Support for this research was provided by NSF under grants AGS-1136269, AGS-1261623, AGS-1242949, and AGS-1259136 and by NASA under contract NNH09CF40C. Computational resources employed for the DNS and LES described here were provided by the DoD HPCMO for related modeling studies of smallscale dynamics, especially ARO contract W911NF-12-C-0097. The authors thank two anonymous reviewers for helpful comments on the manuscript. Researchers wishing to obtain numerical data presented here for collaborative research purposes should contact the lead author.

References

Andreassen, O., P. O. Hvidsten, D. C. Fritts, and S. Arendt (1998), Vorticity dynamics in a breaking gravity wave. Part 1. Initial instability evolution, J. Fluid Mech., 367, 27-46.

Arendt, S., D. C. Fritts, and O. Andreassen (1997), The initial value problem for Kelvin vortex waves, J. Fluid Mech., 344, 181-212.

Arendt, S., D. C. Fritts, and O. Andreassen (1998), Kelvin twist waves in the transition to turbulence, Euro. J. Mech. B/Fluids, 17, 595-604. Baumgarten, G., and D. C. Fritts (2014), Quantifying Kelvin-Helmholtz instability dynamics observed in Noctilucent Clouds: 1. Methods and observations, doi:10.1002/2014JD021832.

Eaton, F., S. A. Mclaughlin, and J. R. Hines (1995), A new frequency-modulated continuous wave radar for studying planetary boundary layer morphology, Radio Sci., 30, 75-88, doi:10.1029/94RS01937.

Franke, P. M., S. Mahmoud, K. Raizada, K. Wan, D. C. Fritts, T. Lund, and J. Werne (2011), Computation of clear-air radar backscatter from numerical simulations of turbulence: 1. Numerical methods and evaluation of biases, J. Geophys. Res., 116, D21101, doi:10.1029/2011JD015895.

Fritts, D. C., and L. Wang (2013), Gravity wave-fine structure interactions. Part 2: Energy dissipation evolutions, statistics, and implications, J. Atmos. Sci., 70, 3735-3755, doi:10.1175/JAS-D-13-059.1.

Fritts, D. C., S. Arendt, and O. Andreassen (1998), Vorticity dynamics in a breaking internal gravity wave. 2. Vortex interactions and transition to turbulence, J. Fluid Mech., 367, 47-65.

Fritts, D. C., C. Bizon, J. A. Werne, and C. K. Meyer (2003), Layering accompanying turbulence generation due to shear instability and gravity wave breaking, J. Geophys. Res., 108(D8), 8452, doi:10.1029/2002JD002406.

Fritts, D. C., L. Wang, J. Werne, T. Lund, and K. Wan (2009a), Gravity wave instability dynamics at high Reynolds numbers. 1: Wave field evolution at large amplitudes and high frequencies, J. Atmos. Sci., 66, 1126-1148, doi:10.1175/2008JAS2726.1.

Fritts, D. C., L. Wang, J. Werne, T. Lund, and K. Wan (2009b), Gravity wave instability dynamics at high Reynolds numbers. 2: Turbulence evolution, structure, and anisotropy, J. Atmos. Sci., 66, 1149-1171, doi:10.1175/2008JAS2727.1.

Fritts, D. C., P. Franke, K. Wan, T. Lund, and J. Werne (2011), Computation of clear-air radar backscatter from numerical simulations of turbulence.

Il: Backscatter moments throughout the lifecycle of a Kelvin-Helmholtz instability, J. Geophys. Res., 116, D11105, doi:10.1029/2010JD014618. Fritts, D. C., K. Wan, P. Franke, and T. Lund (2012), Computation of clear-air radar backscatter from numerical simulations of turbulence. 3. Off-zenith measurements and biases throughout the lifecycle of a Kelvin-Helmholtz instability, J. Geophys. Res., 117, D17101, doi:10.1029/2011JD017179.

Fritts, D. C., L. Wang, and J. Werne (2013), Gravity wave-fine structure interactions. Part 1: Influences of fine-structure form and orientation on flow evolution and instability, J. Atmos. Sci., 70, 3710–3734, doi:10.1175/JAS-D-13-055.1.

Goldberg, R. A., et al. (2004), The MaCWAVE/MIDAS rocket and ground-based measurements of polar summer dynamics: Overview and mean state structure, Geophys. Res. Lett., 31, L24S02, doi:10.1029/2004GL019411.

Hecht, J. H., A. Z. Liu, R. L. Walterscheid, and R. J. Rudy (2005), Maui Mesosphere and Lower Thermosphere (Maui MALT) observations of the evolution of Kelvin-Helmholtz billows formed near 86 km altitude, J. Geophys. Res., 110, D09S10, doi:10.1029/2003JD003908.

Howard, L. (1961), A note on a paper of John W. Miles, J. Fluid Mech., 10, 509-512.

Kelvin, L. (1880), Vibrations of a columnar vortex, Phil. Mag., 10, 155-168.

Klaassen, G. P., and W. R. Peltier (1985). The onset of turbulence in finite-amplitude Kelvin-Helmholtz billows. J. Fluid Mech., 155, 1–35. Lehmacher, G. A., L. Guo, E. Kudeki, P. M. Reyes, A. Akgiray, and J. L. Chau (2007), High-resolution observations of mesospheric layers with the Jicamarca VHF radar, Adv. Space Res., 40(6), 734-743.



- Lübken, F.-J. (1997), Seasonal variation of turbulent energy dissipation rates at high latitudes as determined by in situ measurements of neutral density fluctuations, *J. Geophys. Res.*, 102(D12), 13,441–13,456, doi:10.1029/97JD00853.
- Lübken, F.-J., W. Hillert, G. Lehmacher, and U. von Zahn (1993), Experiments revealing small impact of turbulence on the energy budget of the mesosphere and lower thermosphere, *J. Geophys. Res.*, 98(D11), 20,369–20,384, doi:10.1029/93JD02055.
- Lübken, F.-J., M. Rapp, and P. Hoffman (2002), Neutral air turbulence and temperature in the vicinity of polar mesosphere summer echoes, J. Geophys. Res., 107(D15), 4273, doi:10.1029/2001JD00-0915.
- Miles, J. W. (1961), On the stability of heterogeneous shear flows, J. Fluid Mech., 10, 496-508.
- Palmer, T. L., D. C. Fritts, O. Andreassen, and I. Lie (1994), Three-dimensional evolution of Kelvin-Helmholtz billows in stratified compressible flow, *Geophys. Res. Lett.*, 21, 2287–2290, doi:10.1029/94GL01714.
- Palmer, T. L., D. C. Fritts, and O. Andreassen (1996), Evolution and breakdown of Kelvin-Helmholtz billows in stratified compressible flows. II: Instability structure, evolution, and energetics, *J. Atmos. Sci.*, 53, 3192–3212.
- Pfrommer, T., P. Hickson, and C.-Y. She (2009), A large-aperture sodium fluorescence lidar with very high resolution for mesopause dynamics and adaptive optics studies, *Geophys. Res. Lett.*, 35, L15831, doi:10.1029/2009GL038802.
- Rapp, M., B. Strelnikov, A. Müüllemann, F.-J. Lübken, and D. C. Fritts (2004), Turbulence measurements and implications for gravity wave dissipation during the MaCWAVE/MIDAS summer rocket program, *Geophys. Res. Lett.*, 31, L24S07, doi:10.1029/2003GL019325.
- Thorpe, S. A. (1973), Experiments on instability and turbulence in a stratified shear flow, J. Fluid Mech., 61, 731-751.
- VanZandt, T. E., and D. C. Fritts (1989), A theory of enhanced saturation of the gravity wave spectrum due to increases in atmospheric stability, Pure Appl. Geophys., 130, 399–420.
- Werne, J. A., and D. C. Fritts (2001), Anisotropy in a stratified shear layer, Phys. Chem. Earth (B), 26, 263–268.
- Werne, J., and D. C. Fritts (1999), Stratified shear turbulence: Evolution and statistics, *Geophys. Res. Lett.*, 26, 439–442, doi:10.1029/1999GL900022. Werne, J., T. Lund, B. A. Pettersson-Reif, P. Sullivan, and D. C. Fritts (2005), CAP Phase II Simulations for the Air Force HEL-JTO Project: Atmospheric turbulence simulations on NAVO's 3000-processor IBM P4+ and ARL's 2000-processor Intel Xeon EM64T cluster, 15th DoD HPC User Group Conf., June 2005, Nashville
- Witt, G. (1962), Height, structure and displacements of noctilucent clouds, *Tellus*, 14, 1–18.